

See discussions, stats, and author profiles for this publication at: <https://www.researchgate.net/publication/305038277>

Tandem planet formation for solar system-like planetary systems

Article in *Geoscience Frontiers* · July 2016

DOI: 10.1016/j.gsf.2016.06.011

CITATIONS

3

READS

125

2 authors, including:



Toshikazu Ebisuzaki

RIKEN

412 PUBLICATIONS 5,429 CITATIONS

SEE PROFILE

Some of the authors of this publication are also working on these related projects:



JEM-EUSO [View project](#)



LANFOS [View project](#)

HOSTED BY

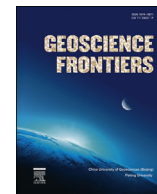


ELSEVIER

Contents lists available at ScienceDirect

China University of Geosciences (Beijing)

Geoscience Frontiers

journal homepage: www.elsevier.com/locate/gsf

Research paper

Tandem planet formation for solar system-like planetary systems

Yusuke Imaeda*, Toshikazu Ebisuzaki

RIKEN, 2-1, Hirosawa, 351-0198, Japan

ARTICLE INFO

Article history:

Received 18 March 2016

Received in revised form

13 June 2016

Accepted 17 June 2016

Available online xxx

Keywords:

Accretion disk

Planet formation

Magneto-rotational instability

Origin of life

ABSTRACT

We present a new united theory of planet formation, which includes magneto-rotational instability (MRI) and porous aggregation of solid particles in a consistent way. We show that the “tandem planet formation” regime is likely to result in solar system-like planetary systems. In the tandem planet formation regime, planetesimals form at two distinct sites: the outer and inner edges of the MRI suppressed region. The former is likely to be the source of the outer gas giants, and the latter is the source for the inner volatile-free rocky planets. Our study spans disks with a various range of accretion rates, and we find that tandem planet formation can occur for $\dot{M} = 10^{-7.3} - 10^{-6.9} M_{\odot} \text{y}^{-1}$. The rocky planets form between 0.4–2 AU, while the icy planets form between 6–30 AU; no planets form in 2–6 AU region for any accretion rate. This is consistent with the gap in the solid component distribution in the solar system, which has only a relatively small Mars and a very small amount of material in the main asteroid belt from 2–6 AU. The tandem regime is consistent with the idea that the Earth was initially formed as a completely volatile-free planet. Water and other volatile elements came later through the accretion of icy material by occasional inward scattering from the outer regions. Reactions between reductive minerals, such as schreibersite (Fe_3P), and water are essential to supply energy and nutrients for primitive life on Earth.

© 2016, China University of Geosciences (Beijing) and Peking University. Production and hosting by Elsevier B.V. This is an open access article under the CC BY-NC-ND license (<http://creativecommons.org/licenses/by-nc-nd/4.0/>).

1. Introduction

The process of planet formation involves growing 1000–10,000 km-sized objects from micron-sized dust grains in the gaseous disk around a newly born star; this disk is formed by the gravitational collapse of a slightly rotating dense molecular cloud (e.g. [Bouvier et al., 2007](#)). Planet formation has been vigorously investigated by many researchers (e.g. [Safronov, 1969](#); [Goldreich and Ward, 1973](#); [Weidenschilling, 1977a](#); [Hayashi et al., 1985](#); [Wetherill and Stewart, 1989](#)) and the core accretion scenario has been generally accepted as the standard model of planet formation. It can be divided into the following steps. First, sub-micron-sized interstellar dust grains grow into cm-sized pebbles through mutual collisions and gradually settle to the midplane of the disk to form a sub-disk of pebbles (e.g. [Weidenschilling, 1977a](#); [Nakagawa et al., 1981](#); [Weidenschilling and Cuzzi, 1993](#)). Second, the pebbles grow into km-sized planetesimals via gravitational instability (e.g. [Safronov, 1969](#); [Hayashi, 1972, 1981](#); [Goldreich and](#)

[Ward, 1973](#); [Hayashi et al., 1985](#)). Third, the gravity of planetesimals causes runaway growth (e.g. [Wetherill and Stewart, 1989](#)), and later oligarchic growth, that results in Mars-sized protoplanets (e.g. [Kokubo and Ida, 1998](#)). Finally, the protoplanets grow further by pebble accretion ([Johansen et al., 2006](#)) and occasional giant impacts ([Kokubo and Ida, 2012](#)). The protoplanets can become gas giants if they reach the critical core mass for trapping gas ($\sim 3\text{--}10 M_{\oplus}$, where M_{\oplus} is the Earth mass) before the gas disk dissipates ([Mizuno, 1980](#); [Pollack et al., 1996](#)); otherwise they remain terrestrial planets ([Chambers and Wetherill, 1998](#)) without gas envelopes (atmospheres).

There are three major difficulties in forming the solar system this way. First, [Weidenschilling \(1977b\)](#) estimated the solid component distribution in the present solar system and found a gap between 2 and 5 AU, which is difficult to explain using the standard model. Second, the eccentricities of the planets in the solar system are small (0.01–0.1). [Kokubo and Ida \(1998\)](#) estimated that the final mass of protoplanets at 1 AU is of the order of a Mars mass (which is about 10 times less massive than Earth). This indicates that ~ 10 Mars-sized objects were distributed in the Earth forming region at the late oligarchic growth stage and that subsequent giant impacts are inevitable for forming the present Earth.

* Corresponding author.

E-mail address: yusuke.imaeda@riken.jp (Y. Imaeda).

Peer-review under responsibility of China University of Geosciences (Beijing).

<http://dx.doi.org/10.1016/j.gsf.2016.06.011>

1674-9871/© 2016, China University of Geosciences (Beijing) and Peking University. Production and hosting by Elsevier B.V. This is an open access article under the CC BY-NC-ND license (<http://creativecommons.org/licenses/by-nc-nd/4.0/>).

Naive consideration gives that the final eccentricities of the planets in such system become significantly large, but this is inconsistent with the present orbit of the Earth. Therefore, given the constraints from planet eccentricities, evolution without giant impacts might be preferable for solar system formation models. Although post giant impact eccentricities may damp due to dynamical friction with the remaining gas disk (Kominami and Ida, 2002) or with residual planetesimals (O'Brien et al., 2006), both are likely to disappear well before the last stage of planet formation.

Finally, the amount of H₂O in the Earth is also difficult to explain. The present oceans mass of the Earth, M_{oce} , is estimated to be 0.023 wt.% of M_{\oplus} . Studies of water and trace elements in the mid-ocean ridge indicate that the upper mantle contains 50–200 ppm water (Michael, 1988; Dixon et al., 2002; Hirschmann, 2006; Maruyama and Okamoto, 2007). This upper mantle water is likely to have been transferred from the surface by plate subduction. From the pre-Cambrian period to the present, the sea level decreased by about 600 m, which corresponds to 0.2 M_{oce} . Maruyama and Liou (2005) and Maruyama et al. (2014) noted that the surface water of the Earth, which was degassed during the magma ocean period, would start to return to the mantle around 750 Ma. In the periods before 750 Ma, the water in the subducting plate returned to the surface because of higher mantle temperature (Maruyama and Okamoto, 2007), including the magma ocean phase. The water reservoirs in the lower mantle (including in the transition zone) and in the core are insignificant (Albarède, 2009) because the material cannot be transported. Therefore, the total amount of H₂O in Earth is less than 0.03% by weight, though some researchers have argued that as much as 10 M_{oce} of water can be stored in the lower mantle (e.g. Genda, 2016) and up to 80 M_{oce} in the core (Nomura et al., 2014).

Ebisuzaki and Imaeda (2016, hereafter paper I) constructed a steady-state, 1-D model of an accretion disk around a newly born star with a specified accretion rate \dot{M} ranging from $10^{-6.5}$ to $10^{-8.0} M_{\odot} \text{ yr}^{-1}$. They showed that the disk consists of three regions: the outer turbulent region (OTR), the magneto-

rotational instability (MRI) suppressed region (MSR), and the inner turbulent region (ITR). Then, they showed that the MSR can be separated in the vertical direction into a quiet area (QA) and turbulent envelopes (see Fig. 1). This picture is consistent with the recent comprehensive review by Armitage (2011). Paper I also found that planet formation actively occurs near the OTR-MSR and MSR-ITR boundaries in the disk model with $\dot{M} = 10^{-7.0} M_{\odot} \text{ yr}^{-1}$. This quantitative model of planet formation was named as the “tandem planet formation” regime because there are two distinct sites for planetary formation in the disk.

This new framework may relax the difficulties faced by previous solar system formation models discussed above. First, because the planets form in two physically separated sites (the outer MRI front near ~ 10 AU and the inner MRI front near ~ 1 AU), it might naturally explain the gap in the distribution of solid material. Second, pebbles are continuously supplied to the formation sites from the outer regions via drift due to the interaction with gas. This results in the formation of fewer large bodies, as shown by Levison et al. (2015). Finally, the temperature of the formation site for rocky planetesimals at the inner MRI front is >1000 K. The rocky planetesimals are therefore expected to lose volatile components including water. This is consistent with the volatile depletion in the terrestrial planets described above. The current volatile components are then added after the solidification of the surface of Earth (Albarède, 2009).

Observational data show that the accretion rates of young stellar objects (with ages of 10^5 – 10^7 years) range from 10^{-10} to $10^{-5} M_{\odot} \text{ yr}^{-1}$ for T-Tauri stars and from 10^{-8} to $10^{-4} M_{\odot} \text{ yr}^{-1}$ for class 0/I stars, which are objects hidden in the dense molecular cloud cores surrounding them (Calvet et al., 2005; Spezzi et al., 2012; Beltrán and de Wit, 2016). Most of the observational data are well represented by simple exponential functions with an e-folding time τ_a , where τ_a ranges 10^5 – 10^7 years and the total accretion mass (time integration of \dot{M}) is $1 M_{\odot}$ (Fig. 2).

In the present paper, we study tandem planet formation in a variety of disks with different accretion rates to investigate the

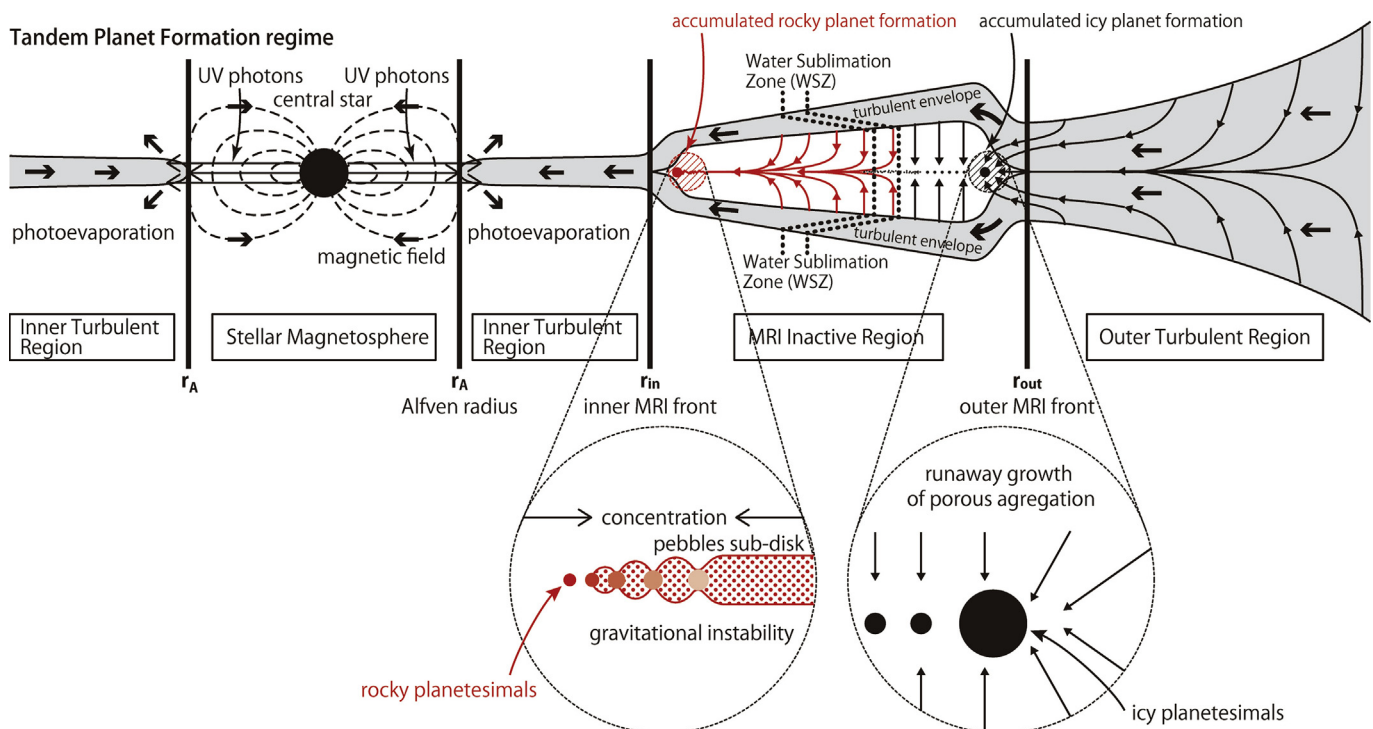


Figure 1. Schematic cross section of the protoplanetary disk proposed in paper I for the tandem planet formation regime. See text for details.

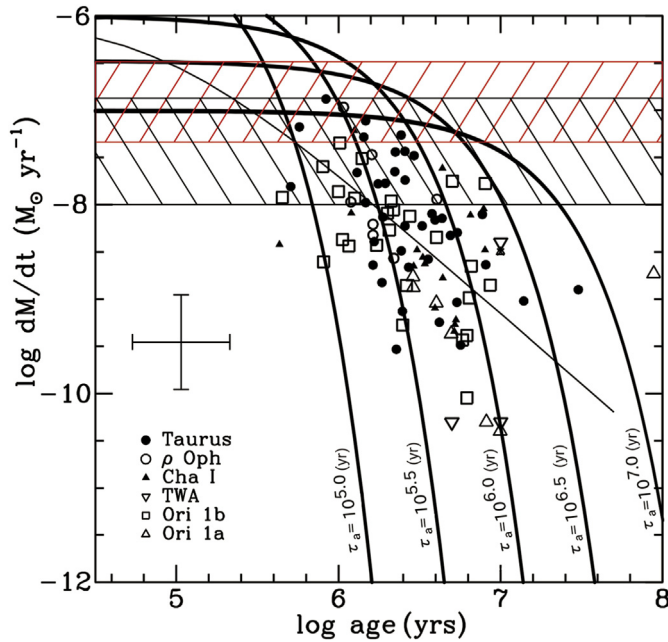


Figure 2. The observation data are plotted in age-accretion rate diagram. This figure was taken from Calvet et al. (2005) and modified so the data can be compared to simple exponential functions with various e-folding times τ_a . The time integral of \dot{M} is set to be $1 M_\odot$. Most of the observational data can be represented by such a function if τ_a is in the range 10^5 – 10^7 yr. The red-hatched and black-hatched areas are the accretion rates for which rocky and icy planet formation can be found in this work.

types of planetary systems that form in this regime. In Section 2 we show the one-dimensional steady state solutions for the accretion disks where particles grow and drift. In Section 3 we calculate the growth of particles from $0.1 \mu\text{m}$ to $\sim 1000 \text{ km}$ size, which corresponds to masses from $\sim 10^{-15} \text{ g}$ to nearly an Earth mass, with the Lagrangian super-particle method. We then compare our results with other models and observations in Section 4.

2. The structure of gas disk

Before presenting the results for particle growth in disks with various accretion rates, we briefly summarize the disk structures obtained in paper I (in which the particles grow and drift). The disk column density, Σ , is related to the accretion rate, \dot{M} , by the standard α -disk prescription (Shakura and Sunyaev, 1973; Lynden-Bell and Pringle, 1974):

$$3\pi\bar{\alpha}c_sH\Sigma = \dot{M} \tag{1}$$

The balance of heating and cooling determines the midplane temperature of the disk, T_m (Kusaka et al., 1970; Hubeny, 1990; Ruden and Pollack, 1991):

$$T_m^4 = \left(\frac{3M\Omega^2}{8\pi\sigma}\right) \left(\frac{3}{8}\frac{\bar{\alpha}}{\alpha_{\text{act}}}\frac{\kappa\Sigma}{2} + \frac{\sqrt{3}}{4}\right) + T_{\text{irr}}^4 \tag{2}$$

$$T_{\text{irr}}^4 = \frac{1}{2}(1-\epsilon)T_*^4\left(\frac{R_*}{r}\right)^2\left[\frac{4}{3\pi}\left(\frac{R_*}{r}\right) + \frac{2}{7}\frac{H}{r}\right] \tag{3}$$

where r is the distance from the central star, α_{act} is the viscous parameter for the MRI active state, $\bar{\alpha}$ is the viscous parameter as a function of the turbulent state, c_s is the sound velocity, H is the scale height of the gas disk, Ω is the angular velocity, σ is the Stefan–Boltzmann constant, κ is the opacity of the gas disk (Stepinski,

1998), T_{irr} is the irradiation temperature due to the central star, ϵ is the albedo of the disk surface (which we take to be 0.5), and T_* and R_* are the temperature and radius of the central star (which we take to be 4000 K and $3R_\odot$). These relationships (Eqs. (1)–(3)) are implicitly coupled with each other.

We consider MRI to be the source of turbulence in the disk (Balbus and Hawley, 1991; Hawley and Balbus, 1991), and take into account the various ionization sources such as thermal ionization (Balbus and Hawley, 2000), galactic cosmic rays, and radionuclides within the disk (Umebayashi and Nakano, 1988). In places where the Elsasser number in the MRI active disk is greater than unity, i.e. $\Lambda = v_{\text{Az}}^2/\eta_0\Omega > 1$, we adopt the viscous parameter $\bar{\alpha} = \alpha_{\text{act}} = 10^{-2.0}$; otherwise, we use $\bar{\alpha} = \alpha_{\text{inact}} = 10^{-2.5}$ to represent the MRI inactive region. In the expression for Λ , v_{Az} is the component of the Alfvén velocity perpendicular to the mid-plane of the disk and η_0 is the Ohmic resistivity. The inner edge of the disk is determined by $r_A = (\mu_*^4/GM_*M^2)^{1/7}$, where G is the gravitational constant, $\mu_* = 10^{36} \text{ G cm}^3$ is the magnetic dipole moment of the central star, and $M_* = 1 M_\odot$ is the mass.

Fig. 3 shows the temperature distribution of the gas disk for different accretion rates. The temperature at $\sim 100 \text{ AU}$ is the same in all cases because heating due to irradiation from the central star dominates over the viscous heating in the outer part of the gas disk. The kink in the temperature distribution near 150–180 K corresponds to the opacity change due to water sublimation (Stepinski, 1998).

Fig. 4 shows the temperature at the outer and inner MRI fronts as a function of \dot{M} . The temperature of the inner MRI front is nearly constant at just above 1000 K, independent of the accretion rate; this is because the temperature is determined by the ionization energy of the alkali metals Na and K (4.431 and 5.139 eV, respectively).

3. Particle growth in the disk

We calculate particle coagulation (Okuzumi et al., 2012; Kataoka et al., 2013), fragmentation (Stewart and Leinhardt, 2009; Wada et al., 2009), drift and sedimentation (Nakagawa et al., 1986), as well as the gravitational instability of the particle sub-disk (Yamoto and Sekiya, 2004) using Lagrange superparticles. Drift velocity in the radial direction, v_{rp} , and sedimentation velocity in the vertical direction, v_{zp} , are given by

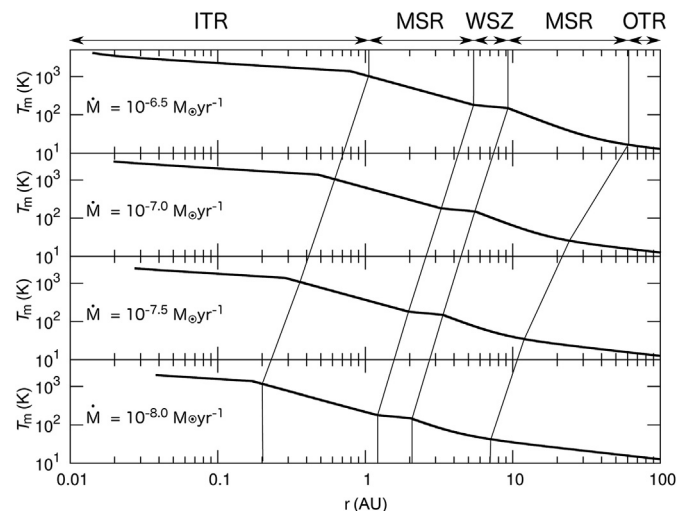


Figure 3. The temperature structure for the gas disk with different accretion rates ($\dot{M} = 10^{-8.0} - 10^{-6.5} M_\odot \text{ yr}^{-1}$). The kink at $T_m = 1380 \text{ K}$ reflects the beginning of olivine sublimation, while the kinks at $T_m = 180 \text{ K}$ and $T_m = 150 \text{ K}$ reflect the end and the beginning of H_2O sublimation.

$$v_{rp} = -\frac{2\Omega t_s}{1 + \Omega^2 t_s^2} \eta r_p \Omega + v_{r,KH} \quad (4)$$

$$v_{zp} = -\frac{\Omega t_s}{1 + \Omega t_s^2} z_p \Omega \quad (5)$$

where the parameter η is

$$\eta = -\frac{1}{2} \left(\frac{c_s}{r_p \Omega} \right)^2 \left(\frac{\partial \ln P_m}{\partial \ln r} \right)_p \quad (6)$$

(r_p, z_p) is the position of the particle, t_s is the particle stopping time due to gas, P_m is the gas pressure at the midplane, and $v_{r,KH}$ is the correction term when the Kelvin–Helmholtz instability occurs in the particle sub-disk. The particle position is updated by these velocities in the gas disk, described in the previous section. The scale height of the particle sub-disk is given by Youdin and Lithwick (2007) to be

$$H_p = \max \left[\left(1 + \frac{\Omega t_s}{\alpha_D} \right)^{-\frac{1}{2}} \left(1 + \frac{\Omega t_s}{\Omega t_s + 1} \right)^{-\frac{1}{2}} H, z_p \right] \quad (7)$$

where α_D is the viscous parameter of the particle sub-disk; this viscous parameter reflects whether the particle is in MRI turbulence, is in Kelvin–Helmholtz turbulence, or in the QA. The condition for gravitational instability is given by

$$\rho_{pm} > 0.78 \frac{M_*}{r_p^3} \quad (8)$$

where $\rho_{pm} = \Sigma_p / \sqrt{2\pi} H_p$ is the particle mass density at the midplane and Σ_p is the particle column density. When this condition is not satisfied, the mass evolution rate of the particle is given by

$$\dot{m}_p = \pi a_p^2 \rho_{pm} v_{rel,pp} \left(1 + \frac{2Gm_p}{a_p v_{rel,pp}^2} \right) \exp\left(-\frac{1}{2}\right) \quad (9)$$

and when the condition is satisfied it is given by Kokubo and Ida (2012):

$$\dot{m}_p = \frac{1}{1.3 \times 10^5} \left(\frac{\Sigma}{2400 \text{ g cm}^{-2}} \right)^{\frac{2}{3}} \left(\frac{m_p}{M_\oplus} \right)^{\frac{2}{3}} \left(\frac{\rho_i}{2 \text{ g cm}^{-3}} \right)^{-\frac{2}{3}} \times \left(\frac{r_p}{1 \text{ AU}} \right)^{-\frac{3}{5}} \left(\frac{\Sigma_p}{10 \text{ g cm}^{-2}} \right) \left(\frac{m_{peb}}{10^{18} \text{ g}} \right)^{-\frac{2}{15}} \left(\frac{M_\oplus}{1 \text{ yr}} \right) \quad (10)$$

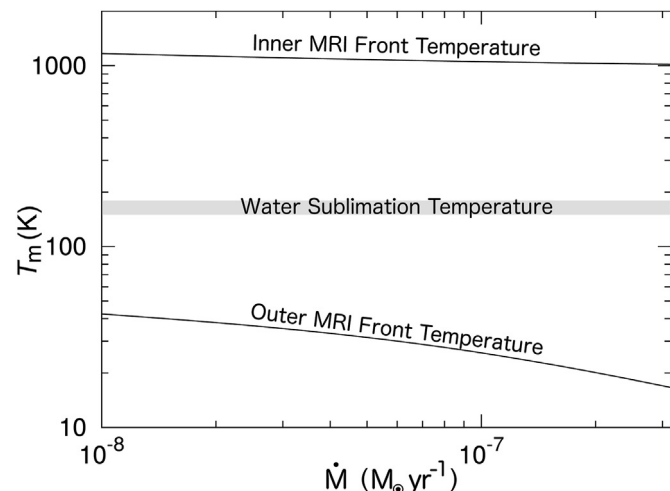


Figure 4. The temperature at the outer and inner MRI fronts as a function of accretion rate.

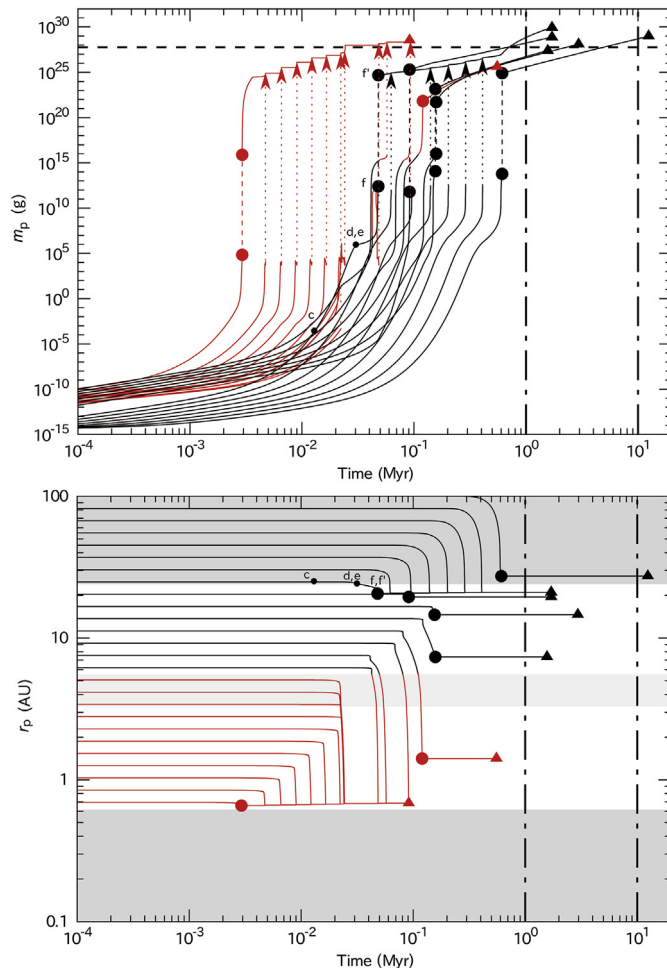


Figure 5. The time evolution of r_p and m_p , starting from different initial distances from the central star. The accretion rate is $\dot{M} = 10^{-7.0} M_\odot \text{ yr}^{-1}$. The filled circles represent the start and the end of gravitational instability, and the triangles represent the end of the calculation (when m_p reaches m_f). The small-filled circles that are accompanied by characters denote important epochs of particle growth (see text).

where $v_{rel,pp}$ is the particle-particle relative velocity given by Ormel and Cuzzi (2007), $a_p = (3m_p/4\pi\rho_i)^{1/3}$ is the particle radius, ρ_i is the particle internal density, m_p is the particle mass, and m_{peb} is the mass in small pebbles around the particle, which is equal to the mass of the particle just before the particle sub-disk reaches gravitational instability. The factor of $e^{-1/2}$ in Eq. (9) is due to the fact that we are evaluating \dot{m} at a height, $z = H_p$, in the particle sub-disk, whose vertical structure is assumed to be $\rho(z) = \rho_{pm} \exp(-z^2/2H_p^2)$.

Fig. 5 shows the time (t) evolution of particles in the $t - r_p$ and $t - m_p$ planes for $\dot{M} = 10^{-7.0} M_\odot \text{ yr}^{-1}$. The black curves indicate particles in the icy region where H_2O is in solid phase; the red curves show particles in the rocky or marginally rocky regions where H_2O is fully or partially in the gas phase. Particle growth starts from a sub-micron-sized monomer, whose radius is $a_p = 0.1 \mu\text{m}$ with an internal density $\rho_i = 1 \text{ g cm}^{-3}$, at an initial location of $(r, z) = (r_s, H)$. Then, particles stick and grow in either a turbulent environment (due to MRI or Kelvin–Helmholtz instability) or a turbulence-free environment. If the particles start in the region where $T_m \geq 150 \text{ K}$, they first grow by mutual collisions. They then begin to drift inward and finally accumulate at the pressure maximum near the inner MRI front to form the volatile-free particle sub-disk, where temperatures are just above 1000 K. Then, gravitational instability occurs in the particle sub-disk and

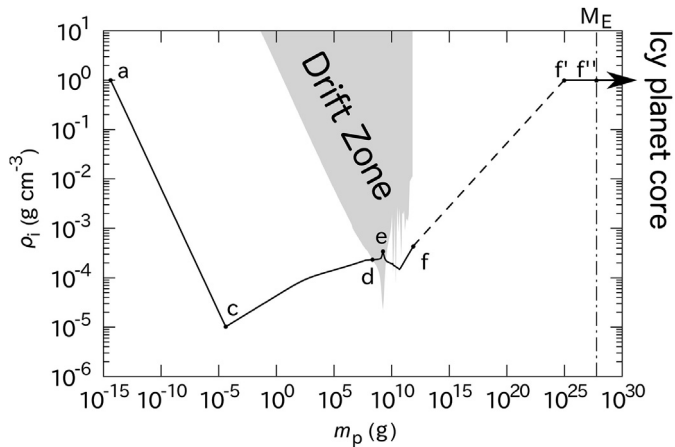


Figure 6. The internal density evolution of the particle starting from 26 AU. The dashed line represents the gravitational instability of the particle sub-disk. The shaded area represents the “drift zone”, where particle drift is considerable. The attached letters denote important epochs in the particle growth (see text for more details).

planetesimals form. The planetesimals grow further by mutual collisions and the accretion of pebbles ($\sim 10^4$ g), which are continuously supplied from further out in the disk (≤ 10 AU), to become terrestrial protoplanets.

Particles starting from beyond the outer MRI front evolve in a different way. As shown in Fig. 6, the resultant aggregates are porous, with densities as low as 10^{-5} g cm $^{-3}$ (see also Okuzumi et al., 2012; Kataoka et al., 2013). The internal density of a particle, ρ_i , first decreases as a ballistic cluster-cluster aggregate (BCCA) until the compression energy due to the ram pressure from surrounding gas overcomes the rolling energy of two contacting monomers (points a to c in Fig. 6). Then, the internal density gradually increases due to compression of the gas by ram pressure. The particle then begins to drift inward when the particle mass reaches $m_p \sim 10^8$ g because the radial drift timescale becomes shorter than the growth timescale (point d in Fig. 6). Next, the particles drift into the QA at $r = r_{\text{out}}$ (point e), and settle to the disk midplane to form a particle sub-disk of thickness H_p (Nakagawa et al., 1986; Youdin and Lithwick, 2007). For the labeling of each epoch, see also Figs. 5 and 6. When the density of the solid particles dominates over that of the gas, the Kelvin–Helmholtz instability occurs, preventing the particle sub-disk from becoming thin enough for the gravitational instability of the particle sub-disk. However, even in such turbulence, the particles continue to grow by sticking and are gradually decoupled from the gas. As the result, the particle sub-disk becomes thin enough for gravitational instability to occur to form planetesimals. As in the previous case, these planetesimals then grow through mutual collisions and the accretion of pebbles (Ormel and Klahr, 2010; Lambrechts and Johansen, 2012). Therefore, rocky planets and icy planets form at two distinct planet formation sites; this is described in paper I as tandem planet formation.

At the inner MRI front, a particle reaches M_{\oplus} at $t_E = 0.024$ Myr, eventually reaching a final mass $m_f = 5.5 M_{\oplus}$ by 0.091 Myr at 0.69 AU (see also Table 1). Here, $m_f = 2\pi\Sigma_p r_p r_H$ is the mass of the particle sub-disk within the annulus of one Hill radius (r_H) in width centered at r_p , and t_E is the time that the planet reaches one Earth mass. On the other hand, a particle grows to M_{\oplus} by 0.7 Myr at the outer MRI front, eventually achieving a mass of $140M_{\oplus}$ by 1.7 Myr at a distance of 21 AU.

Fig. 7 shows the evolution diagram for particles in the case of a higher accretion rate ($\dot{M} = 10^{-6.5} M_{\odot} \text{yr}^{-1}$). The MRI fronts shift outward because the higher accretion rates mean that the column density is larger. Planet formation at the inner MRI front (red

Table 1
Summary of planetary formation.

	$\log \dot{M} (M_{\odot} \text{yr}^{-1})$	$t_{\text{acc}} (\text{Myr})^a$	$t_E (\text{Myr})$	$r_p (\text{AU})$	$m_f (M_{\oplus})$
Outer MRI Front	-6.9	0.79	0.46	24	130
			0.76	25	130
	-7.0	1.0	0.71	21	140
			0.70	19	12
	-7.1	1.3	0.80	19	84
	-7.2	1.6	0.86	16	50
	-7.3	2.0	0.89	13	30
	-7.4	2.5	0.81	12	30
			1.2	11	1.2
		-7.5	3.2	0.97	11
Inner MRI Front	-7.6	4.0	0.94	9.4	10
	-7.7	5.0	1.0	8.6	10
	-7.8	6.3	1.1	7.4	5.9
	-7.9	7.9	1.1	7.1	5.5
	-8.0	10	1.1	6.1	3.4
	-6.5	0.32	0.050	1.2	15
	-6.6	0.40	0.043	1.1	21
	-6.7	0.50	0.041	0.95	7.8
	-6.8	0.63	0.033	0.86	17
	-6.9	0.79	0.037	0.77	9.7
-7.0	1.0	0.024	0.69	5.5	
-7.1	1.3	0.029	0.61	4.9	
-7.2	1.6	0.037	0.55	2.8	
-7.3	2.0	0.033	0.49	2.0	

^a $t_{\text{acc}} = 0.1 M_{\odot} / \dot{M}$.

curves) is essentially unchanged; the planet eventually reaches $\sim 15M_{\oplus}$ by 0.12 Myr at 1.2 AU (Table 1). However, the growth of icy planets at the outer MRI front is considerably slower; the planets cannot reach M_{\oplus} by $t = t_{\text{acc}} = 0.1 M_{\odot} / \dot{M}$. If we do not care about the duration of mass accretion, the planet can reach $\sim 890M_{\oplus}$ after 2.8 Myr, but the amount of mass accreted onto the central star becomes large (as high as $\sim 0.89M_{\odot}$) in such case; this is not acceptable for a model of solar system formation.

Figs. 8 and 9 show cases with lower accretion rates ($\dot{M} = 10^{-7.5}$ and $10^{-8.0} M_{\odot} \text{yr}^{-1}$). The tandem nature of planet formation is basically preserved for the case of $\dot{M} = 10^{-7.5} M_{\odot} \text{yr}^{-1}$, although the final mass of the rocky planet at the inner MRI front is as low as $0.52M_{\oplus}$. For the case of $\dot{M} = 10^{-8.0} M_{\odot} \text{yr}^{-1}$, the rocky planet reaches only $\sim 0.1M_{\oplus}$, although icy planets can reach M_{\oplus} by 1 Myr.

4. Discussion

Tandem planet formation takes place vigorously in disks with $\dot{M} = 10^{-6.9} - 10^{-7.3} M_{\odot} \text{yr}^{-1}$, as can be seen in Figs. 10 and 11. Both rocky planets (red dots) and icy planets (black dots) successfully grow to M_{\oplus} within $t_{\text{acc}} = 0.1 M_{\odot} / \dot{M}$ at the outer and inner MRI fronts. At higher accretion rates, e.g. $\dot{M} = 10^{-6.5} M_{\odot} \text{yr}^{-1}$, the outer MRI front shifts considerably outward, and the growth of planets at the outer MRI front tends to be too slow to match t_{acc} ; however, the rocky planets grow using the abundant material supplied from the outer region ($r = 1 - 10$ AU) to the inner MRI front. On the other hand, at low accretion rates (less than $\dot{M} = 10^{-8.0} M_{\odot} \text{yr}^{-1}$), the icy planets grow rapidly because the outer MRI front shifts inward, but the rocky planets cannot grow to M_{\oplus} because insufficient material is supplied and the final mass becomes $m_f < M_{\oplus}$.

In Fig. 2, the red and black hatched regions represent the range of accretion rates for rocky planet formation and icy planet formation, respectively. Because many young stellar objects have accretion rates that fall in this hatched region, tandem planet formation is likely to take place in the disks around these objects. These regions also correspond to ages of $t = 1 - 30$ Myr, and planet formation finishes by 30 Myr, most likely within 3–10 Myr.

The right panel of Fig. 10 shows the solid component distribution observed in the present solar system. This distribution reflects

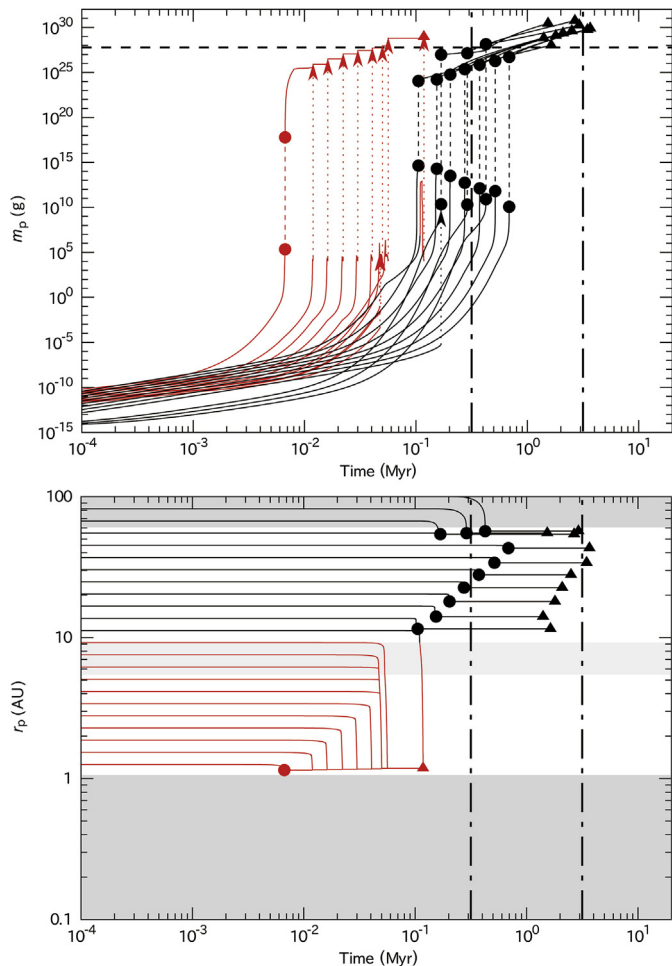


Figure 7. The same diagram as Fig. 5, but for $\dot{M} = 10^{-6.5} M_{\odot} \text{ yr}^{-1}$.

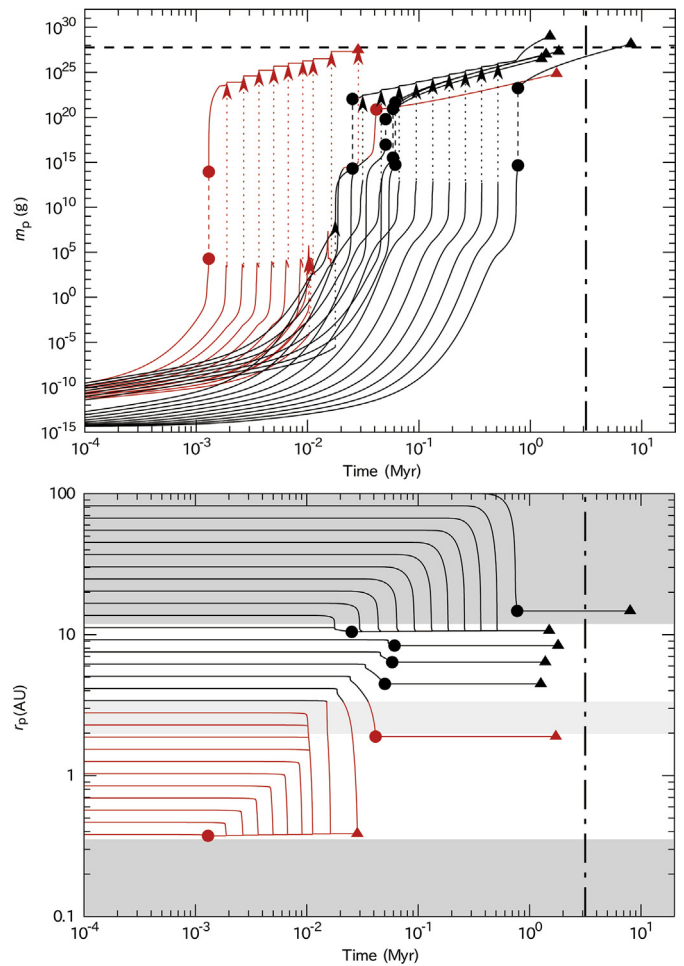


Figure 8. The same diagram as Fig. 5, but for $\dot{M} = 10^{-7.5} M_{\odot} \text{ yr}^{-1}$.

the fact that the mass of Mars is $0.1M_{\oplus}$ and that the total mass in the asteroid belt is as low as $10^{-3}M_{\oplus}$ (Weidenschilling, 1977b). Such a gap in the distribution of solid particles is the key to reproducing a planetary system like our solar system. In fact, the major motivation of the so called “Grand Tack model” (Walsh et al., 2011; Walsh and Morbidelli, 2011) was the formation of such a gap in the planetesimal distribution by the tacking of the gas giants, Jupiter and Saturn. The Grand Tack model assumes that Jupiter forms first and migrates inward to 1.5–2 AU. Then, Saturn grows and migrates as well until it becomes locked in a 2:3 resonance with Jupiter. The resonant pair of planets then migrate outward to 5 and 7 AU. Gravitational scattering of planetesimals by Jupiter influences the inward migration, and the scattered planetesimals eventually coalesce into a narrow torus around 1 AU. This Grand Tack model has become very popular.

However, the Grand Tack model faces at least three difficulties, as discussed below. First, as can be seen in Figs. 5, 7–9 and Table 1, rocky planets near the inner MRI fronts always form earlier than the icy planets near the outer MRI front; this is consistent with many other planet formation calculations (e.g. Hayashi et al., 1985). The “Jupiter first” initial condition, which is required by the Grand Tack model, is thus quite unlikely. Second, the model can create a gap from 2–7 AU, but it cannot clear the inner region at less than 0.7 AU, where the solar system solid component distribution also shows a significant deficit (as seen in Fig. 10). Third, and most importantly, the inner rocky planets will inevitably become wet in the Grand Tack model, because the tacking Jupiter scatters volatile-

rich planetesimals/asteroids into the inner solar system. In contrast, the silicate samples obtained for the Earth, the Moon, and Mars consistently show that their mantle materials are water poor, as we discussed in the introduction; this implies that they were born as volatile-free planets (Albarède, 2009; Maruyama et al., 2013). It is believed that water and other volatiles were added to the inner planets in a very late phase (after the surfaces solidified) through the bombardment of volatile rich asteroids/planetesimals (Carr and Waenke, 1992; Albarède, 2009; Sharp et al., 2010). The two-step formation model, in which a highly reductive planet is first born completely volatile-free, and the advent of bio-elements occurs distinctively later (ABEL bombardment) to form an oxidized planet with an ocean and an atmosphere, is referred as the ABEL model in Maruyama and Ebisuzaki (2016). In this case, the reactions of reductive minerals, such as schreibersite (Fe_3P), with water is essential to supply energy and nutrients for the primitive stages of life (e.g. Ebisuzaki and Maruyama, 2015).

Unlike the Grand Tack model, tandem planet formation can naturally explain the gap in the distribution of the solid components seen in the right panel of Fig. 10 (Weidenschilling, 1977b). In fact, one can see a distinct gap between the distribution of rocky planets (red histogram: 0.4–2 AU) and that of icy planets (black histogram: 6–30 AU); no formation of planetesimals/planets occurs in the range of 2–6 AU. The trapping of solid particles at the inner MRI fronts (0.7–2 AU) also naturally explains the deficit of solid components in the inner region of the solar system at less than 0.6 AU.

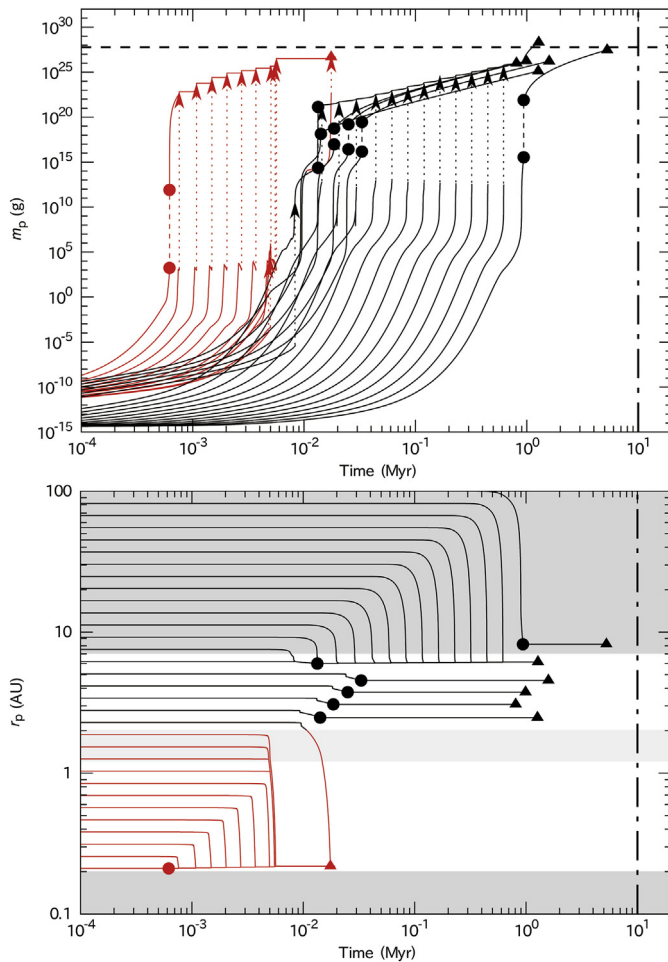


Figure 9. The same diagram as Fig. 5, but for $\dot{M} = 10^{-8.0} M_{\odot} \text{ yr}^{-1}$.

Furthermore, tandem planet formation is compatible with the reported compositional distribution in the asteroid belt (DeMeo and Carry, 2014). Fig. 12 shows a possible scenario for solar system-like systems. At early stages of accretion, rocky planet formation is initiated at the inner MRI front while icy planet formation

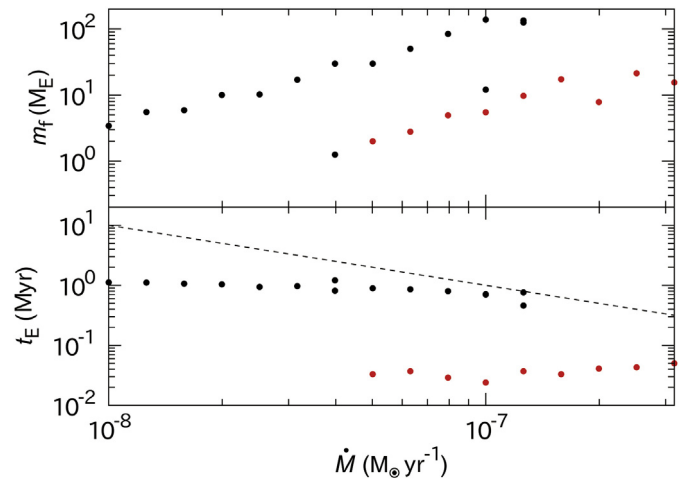


Figure 11. The final mass m_f (top panel) and the time t_E at which the planet reaches M_{\oplus} (bottom panel) plotted against \dot{M} for icy (black) and rocky (red) planets. The dashed line in the bottom panel represents the condition of $t_E = t_{\text{acc}}$.

is not yet active (Fig. 12a). As the accretion rate decreases, tandem planet formation takes place. The planets or planet cores form one by one as MRI fronts shift inward (Fig. 12b, c). The gas in the inner part of the disk starts to disappear due to ionization from the central star (Fig. 12d), and the residual rocky planetesimals, which suffer thermal alterations from radiation, are scattered by the inner planets (Fig. 12e). After the gas disperses in the outer region of the disk, the residual icy planetesimals are scattered by the gas giants (Fig. 12f) to form the present solar system (Fig. 12g). The resulting asteroid belt objects are a mixture of those from the inner MRI front (rocky, thermally metamorphosed composition) and from the outer MRI front (icy, primitive chemical composition), which are scattered into the asteroid belt by gravitational interaction with larger objects, like protoplanets.

Many questions, of course, remain for future studies. Among them, determining how the tandem planet formation depends on the vertical magnetic field of the gas disk is the most important. In preliminary calculations, we found that the tandem planet formation regime does not occur when the magnetic field of the disk is considerably weaker (by a factor of 5) because the outer MRI front

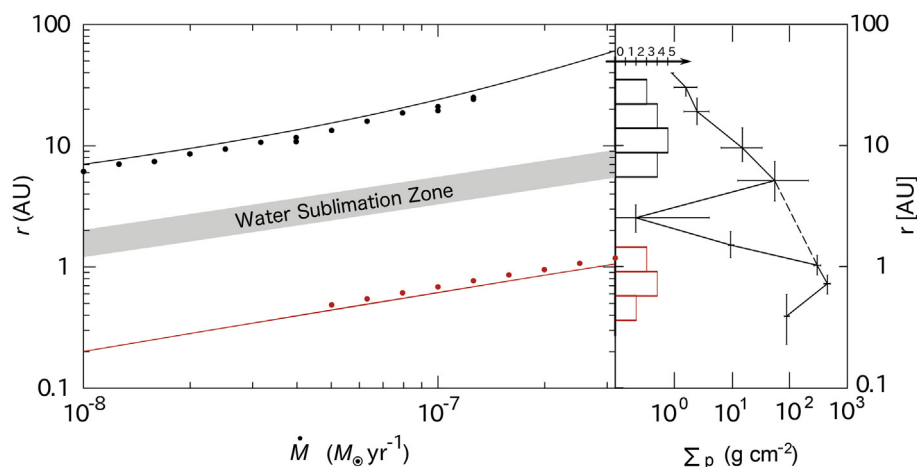


Figure 10. The left panel shows the locations of the inner (red curve) and outer (black curve) MRI fronts as well as the water sublimation zone (WSZ; gray shade). The sublimation temperature of H_2O corresponds to $150 \text{ K} < T_m < 180 \text{ K}$. Dots represent the locations of the icy (black) and rocky (red) planets that successfully grew to M_{\oplus} within $t_{\text{acc}} = 0.1 M_{\odot} / \dot{M}$. Tandem planet formation is active for accretion rates ranging from $\dot{M} = 10^{-7.3}$ to $10^{-6.9} M_{\odot} \text{ yr}^{-1}$. The right panel shows the solid component distribution observed in the present solar system (figure scanned and altered from Weidenschilling (1977b)). The gap noted by Weidenschilling (1977b) likely corresponds to the region between the water sublimation zone. The planet distribution (black and red histograms) in r is consistent with the gap observed in the solar system.

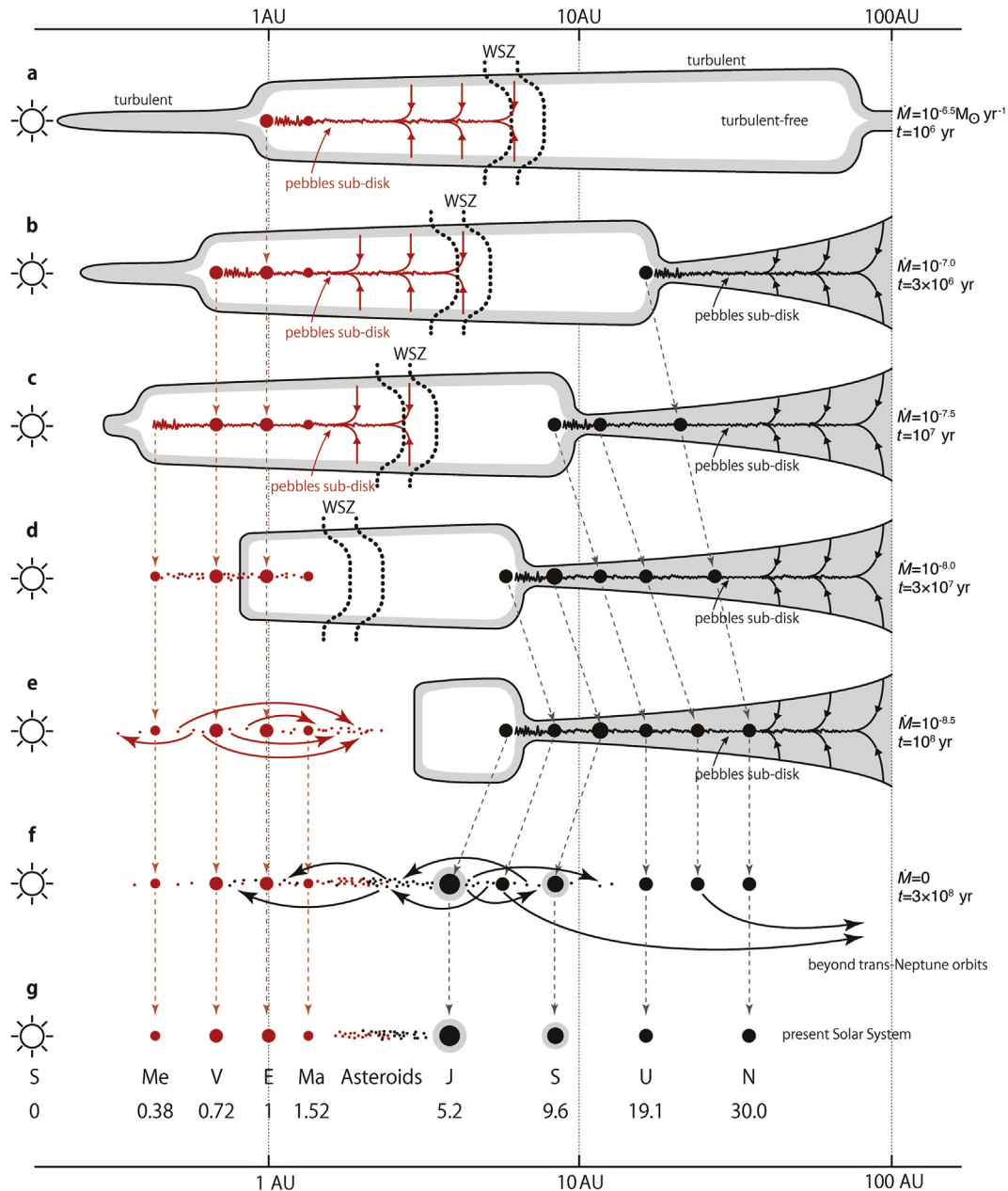


Figure 12. A possible scenario for the formation of solar system-like systems. Each panel is a different epoch: (a) Rocky planet formation around the inner MRI front was initiated when \dot{M} is as high as $10^{-6.5} M_{\odot} \text{yr}^{-1}$. (b) Icy planet formation around the outer MRI front began as \dot{M} decreases. (c) Planets or planets cores formed one by one near the MRI fronts. (d) The ionizing radiation and the stellar wind from the central star dissipated the gas in the inner part of the disk. (e) Residual rocky planetesimals were scattered by the rocky planets. (f) Residual icy planetesimals were scattered by the gas giants. (g) The present solar system.

shifts outward beyond 100 AU. We plan to explore the particle growth in such a case in the near future. Such cases might explain the variations in planet distributions with the magnetic fields and angular momenta of the parent molecular clouds, though this is beyond the scope of the present work.

The last stage of the formation process in the tandem planet formation regime must also be explored more precisely through both population-synthesis simulations (e.g. [Sasaki and Ebisuzaki, in press](#)) and N-body simulations. In the later stages, the situation becomes more complex than what we have modeled due to many factors such as the depletion of pebbles, the saturation of planetesimal growth due to gravitational heating of planetesimals, and the various types of planetary migrations.

Acknowledgments

We thank Prof. S. Maruyama for his continuous encouragement and Dr. James Dohm for improving the language in the manuscript. This work was partially supported by Grant-in-Aid for Scientific Research on Innovative Areas Number 26106006.

References

- Albarède, F., 2009. Volatile accretion history of the terrestrial planets and dynamic implications. *Nature* 461, 1227–1233.
- Armitage, P.J., 2011. Dynamics of protoplanetary disks. *Annual Review of Astronomy and Astrophysics* 49, 195–236.

- Balbus, S., Hawley, J., 2000. Solar nebula magnetohydrodynamics. *Space Science Reviews* 92 (1–2), 39–54.
- Balbus, S.A., Hawley, J.F., 1991. A powerful local shear instability in weakly magnetized disks. I – Linear analysis. *The Astrophysical Journal* 376, 214–222.
- Beltrán, M.T., de Wit, W.J., 2016. Accretion disks in luminous young stellar objects. *The Astronomy and Astrophysics Review* 24, 6.
- Bouvier, J., Alencar, S.H.P., Bouvier, T., Dougados, C., Balog, Z., Grankin, K., Hodgkin, S.T., Ibrahimov, M.A., Kun, M., Magakian, T. Yu., Pinte, C., 2007. Magnetospheric accretion-ejection processes in the classical T tauri star AA tauri. *Astronomy and Astrophysics* 463 (3), 1017–1028.
- Calvet, N., Briceño, C., Hernández, J., Hoyer, S., Hartmann, L., Sicilia-Aguilar, A., Megeath, S.T., D'Alessio, P., 2005. Disk evolution in the Orion OB1 Association. *The Astronomical Journal* 129, 935–946.
- Carr, M.H., Waenke, H., 1992. Earth and Mars – Water inventories as clues to accretional histories. *Icarus* 98, 61–71.
- Chambers, J.E., Wetherill, G.W., 1998. Making the terrestrial planets: N-body integrations of planetary embryos in three dimensions. *Icarus* 136, 304–327.
- DeMeo, F.E., Carry, B., 2014. Solar System evolution from compositional mapping of the asteroid belt. *Nature* 505, 629–634.
- Dixon, J.E., Leist, L., Langmuir, C., Schilling, J.-G., 2002. Recycled dehydrated lithosphere observed in plume-influenced mid-ocean-ridge basalt. *Nature* 420, 385–389.
- Ebisuzaki, T., Imaeda, Y., 2016. United Theory of Planet Formation (I): Tandem Regime (Paper I). ArXiv e-prints, 1601.05509.
- Ebisuzaki, T., Maruyama, S., 2015. United theory of biological evolution: Disaster-forced evolution through Supernova, radioactive ash fall-outs, genome instability, and mass extinctions. *Geoscience Frontiers* 6 (1), 103–119.
- Genda, H., 2016. Origin of earth's oceans: an assessment of the total amount, history and supply of water. *Geochemical Journal* 50 (1), 27–42.
- Goldreich, P., Ward, W.R., 1973. The formation of planetesimals. *The Astrophysical Journal* 183, 1051–1062.
- Hawley, J.F., Balbus, S.A., 1991. A powerful local shear instability in weakly magnetized disks. II. Nonlinear evolution. *The Astrophysical Journal* 376, 223–233.
- Hayashi, C., 1972. Origin of the solar system (in Japanese). In: Report of 5-th Symposium on Moon and Planets at the Institute of Space and Aeronautics, p. 13.
- Hayashi, C., 1981. Structure of the solar nebula, growth and decay of magnetic fields and effects of magnetic and turbulent viscosities on the nebula. *Progress of Theoretical Physics Supplement* 70, 35–53.
- Hayashi, C., Nakazawa, K., Nakagawa, Y., 1985. Formation of the solar system. In: Black, D.C., Matthews, M.S. (Eds.), *Protostars and Planets II*, pp. 1100–1153.
- Hirschmann, M.M., 2006. Water, melting, and the deep earth H₂O cycle. *Annual Review of Earth and Planetary Sciences* 34 (1), 629–653.
- Hubeny, I., 1990. Vertical structure of accretion disks – A simplified analytical model. *The Astrophysical Journal* 351, 632–641.
- Johansen, A., Klahr, H., Henning, T., 2006. Gravitoturbulent formation of planetesimals. *The Astrophysical Journal* 636, 1121–1134.
- Kataoka, A., Tanaka, H., Okuzumi, S., Wada, K., 2013. Fluffy dust forms icy planetesimals by static compression. *Astronomy and Astrophysics* 557, L4.
- Kokubo, E., Ida, S., 1998. Oligarchic growth of protoplanets. *Icarus* 131, 171–178.
- Kokubo, E., Ida, S., 2012. Dynamics and accretion of planetesimals. *Progress of Theoretical and Experimental Physics* 2012 (1), 01A308.
- Kominami, J., Ida, S., 2002. The effect of tidal interaction with a gas disk on formation of terrestrial planets. *Icarus* 157, 43–56.
- Kusaka, T., Nakano, T., Hayashi, C., 1970. Growth of solid particles in the primordial solar nebula. *Progress of Theoretical Physics* 44, 1580–1595.
- Lambrechts, M., Johansen, A., 2012. Rapid growth of gas-giant cores by pebble accretion. *Astronomy and Astrophysics* 544, A32.
- Levison, H.F., Kretke, K.A., Duncan, M.J., 2015. Growing the gas-giant planets by the gradual accumulation of pebbles. *Nature* 524, 322–324.
- Lynden-Bell, D., Pringle, J.E., 1974. The evolution of viscous discs and the origin of the nebular variables. *Monthly Notices of the Royal Astronomical Society* 168, 603–637.
- Maruyama, S., Ebisuzaki, T., 2016. Origin of the Earth: a Proposal of New Model Called Abel. *Geoscience Frontiers* (Submitted).
- Maruyama, S., Ikoma, M., Genda, H., Hirose, K., Yokoyama, T., Santosh, M., 2013. The naked planet earth: most essential pre-requisite for the origin and evolution of life. *Geoscience Frontiers* 4, 141–165.
- Maruyama, S., Liou, J.G., 2005. From snowball to phanerozoic earth. *International Geology Review* 47 (8), 775–791.
- Maruyama, S., Okamoto, K., 2007. Water transportation from the subducting slab into the mantle transition zone. *Gondwana Research* 11 (12), 148–165.
- Maruyama, S., Sawaki, Y., Ebisuzaki, T., Ikoma, M., Omori, S., Komabayashi, T., 2014. Initiation of leaking earth: an ultimate trigger of the cambrian explosion. *Gondwana Research* 25 (3), 910–944.
- Michael, P.J., 1988. The concentration, behavior and storage of H₂O in the suboceanic upper mantle: implications for mantle metasomatism. *Geochimica et Cosmochimica Acta* 52 (2), 555–566.
- Mizuno, H., 1980. Formation of the giant planets. *Progress of Theoretical Physics* 64, 544–557.
- Nakagawa, Y., Nakazawa, K., Hayashi, C., 1981. Growth and sedimentation of dust grains in the primordial solar nebula. *Icarus* 45, 517–528.
- Nakagawa, Y., Sekiya, M., Hayashi, C., 1986. Settling and growth of dust particles in a laminar phase of a low-mass solar nebula. *Icarus* 67, 375–390.
- Nomura, R., Hirose, K., Uesugi, K., Ohishi, Y., Tsuchiyama, A., Miyake, A., Ueno, Y., 2014. Low core-mantle boundary temperature inferred from the solidus of pyrolyte. *Science* 343, 522–525.
- O'Brien, D.P., Morbidelli, A., Levison, H.F., 2006. Terrestrial planet formation with strong dynamical friction. *Icarus* 184, 39–58.
- Okuzumi, S., Tanaka, H., Kobayashi, H., Wada, K., 2012. Rapid coagulation of porous dust aggregates outside the snow line: a pathway to successful icy planetesimal formation. *The Astrophysical Journal* 752, 106.
- Ormel, C.W., Cuzzi, J.N., 2007. Closed-form expressions for particle relative velocities induced by turbulence. *Astronomy and Astrophysics* 466, 413–420.
- Ormel, C.W., Klahr, H.H., 2010. The effect of gas drag on the growth of protoplanets. Analytical expressions for the accretion of small bodies in laminar disks. *Astronomy and Astrophysics* 520, A43.
- Pollack, J.B., Hubickyj, O., Bodenheimer, P., Lissauer, J.J., Podolak, M., Greenzweig, Y., 1996. Formation of the giant planets by concurrent accretion of solids and gas. *Icarus* 124, 62–85.
- Ruden, S.P., Pollack, J.B., 1991. The dynamical evolution of the protosolar nebula. *The Astrophysical Journal* 375, 740–760.
- Safronov, V.S., 1969. *Evolution of the Protoplanetary Cloud and Formation of the Earth and the Planets*. Nauka, Moscow (translated by Israel program for scientific translations, Keter press, Jerusalem). (Also by NASA TTF-677).
- Sasaki, T., Ebisuzaki, T., 2016. Population synthesis of planet formation using a torque formula with dynamic effects. *Geoscience Frontiers* (in press), <http://dx.doi.org/10.1016/j.gsf.2016.04.002>.
- Shakura, N.I., Sunyaev, R.A., 1973. Black holes in binary systems. Observational appearance. *Astronomy and Astrophysics* 24, 337–355.
- Sharp, Z.D., Shearer, C.K., McKeegan, K.D., Barnes, J.D., Wang, Y.Q., 2010. The chlorine isotope composition of the Moon and Implications for an anhydrous mantle. *Science* 329, 1050–1053.
- Spezzi, L., de Marchi, G., Panagia, N., Sicilia-Aguilar, A., Ercolano, B., 2012. Photometric determination of the mass accretion rates of pre-mainsequence stars – III. Results in the large magellanic cloud. *Monthly Notices of the Royal Astronomical Society* 421, 78–97.
- Stepinski, T.F., 1998. The solar nebula as a process—An analytic model. *Icarus* 132, 100–112.
- Stewart, S.T., Leinhardt, Z.M., 2009. Velocity-dependent catastrophic disruption criteria for planetesimals. *The Astrophysical Journal Letters* 691, L133–L137.
- Umebayashi, T., Nakano, T., 1988. Ionization state and magnetic fields in the solar nebula. *Progress of Theoretical Physics Supplement* 96, 151–160.
- Wada, K., Tanaka, H., Suyama, T., Kimura, H., Yamamoto, T., 2009. Collisional growth conditions for dust aggregates. *The Astronomical Journal* 702 (2), 1490–1501.
- Walsh, K.J., Morbidelli, A., 2011. The effect of an early planetesimal-driven migration of the giant planets on terrestrial planet formation. *Astronomy and Astrophysics* 526, A126.
- Walsh, K.J., Morbidelli, A., Raymond, S.N., O'Brien, D.P., Mandell, A.M., 2011. A low mass for Mars from Jupiter's early gas-driven migration. *Nature* 475, 206–209.
- Weidenschilling, S.J., 1977b. The distribution of mass in the planetary system and solar nebula. *Astrophysics and Space Science* 51 (1), 153–158.
- Weidenschilling, S.J., 1977a. Aerodynamics of solid bodies in the solar nebula. *Monthly Notices of the Royal Astronomical Society* 180, 57–70.
- Weidenschilling, S.J., Cuzzi, J.N., 1993. Formation of planetesimals in the solar nebula. In: Levy, E.H., Lunine, J.I. (Eds.), *Protostars and Planets III*, pp. 1031–1060.
- Wetherill, G.W., Stewart, G.R., 1989. Accumulation of a swarm of small planetesimals. *Icarus* 77, 330–357.
- Yamato, F., Sekiya, M., 2004. The gravitational instability in the dust layer of a protoplanetary disk: axisymmetric solutions for nonuniform dust density distributions in the direction vertical to the midplane. *Icarus* 170, 180–192.
- Youdin, A.N., Lithwick, Y., 2007. Particle stirring in turbulent gas disks: including orbital oscillations. *Icarus* 192, 588–604.